Power System Technology
Volume 50, No. 1, 2026
ISSN: 1000-3673

# Twin-View: A Hybrid MRI Analysis Framework for Integrated Brain Tumor Segmentation and Classification

**Bijoy Kumer Karmaker,**
Department of Electrical and Electronic Engineering, Jatiya Kabi Kazi Nazrul Islam University, Trishal, Mymensingh, Bangladesh
**Pranjal Chakraborty Parbo**
Department of Electrical and Electronic Engineering, Jatiya Kabi Kazi Nazrul Islam University, Trishal, Mymensingh, Bangladesh
**Kazi Md. Shahiduzzaman**
Department of Electrical and Electronic Engineering, Jatiya Kabi Kazi Nazrul Islam University, Trishal, Mymensingh, Bangladesh
**Md. Mahbubur Rahman**
Department of Electrical and Electronic Engineering, Jatiya Kabi Kazi Nazrul Islam University, Trishal, Mymensingh, Bangladesh
**Ileas Pramanik**
Department of Computer Science and Engineering, Begum Rokeya University, Rangpur, Bangladesh

**Abstract**

Accurate detection of brain tumors is vital for effective clinical diagnosis and treatment planning. However, manual detection is challenging and time-consuming due to the wide variability in tumor images, which differ in shape and texture. Magnetic Resonance Imaging (MRI) is a common modality used for detecting brain tumors. An automated approach is essential for precise tumor identification. This paper introduces a hybrid framework called Twin-View that utilizes machine learning and deep learning techniques to both segment and classify brain tumors from 2D MRI data. The model was trained and evaluated on 7,023 T1 and T2-weighted contrast-enhanced MRI images, categorized into four classes: glioma, meningioma, pituitary tumor, and non-tumor. The proposed approach uses ResNet50, K-Nearest Neighbors (KNN), Support Vector Machine (SVM), and Random Forest for comparative classification, while a hybrid segmentation model integrates Random Forest with a U-Net architecture. The ResNet50 model achieved an accuracy of 94% on its own. The final hybrid model can assist medical practitioners in verifying the presence, location, and type of a brain tumor, thereby accelerating the treatment procedure.

**Key Words:** Brain tumor, MRI, Deep learning, U-Net, ResNet50, Machine learning, Segmentation, Classification.

## 1. Introduction

A tumor is a mass or tissue formation resulting from uncontrolled cell division. Tumors can develop in several physiological structures, including muscles, connective tissues, glands, and organs. There exist two categories of tumors: benign and malignant. Benign tumors remain localized and do not metastasize to other regions of the body.

They do not disseminate to distant organs or adjacent tissues. Benign tumors generally have distinct margins and exhibit gradual growth [1–3]. They generally possess a fibrous capsule and exhibit slow growth. Malignant tumors, capable of infiltrating adjacent tissues, disseminating via metastasis to distant sites, and proliferating uncontrollably, are classified as malignant [4]. They may also produce a range of symptoms. In 2002, the Central Brain Tumor Registry of the United States (CBTRUS) documented around 39,550 new instances of primary benign and malignant brain tumors. The results indicate that there are 14 primary brain tumors recorded per 100,000 individuals, regardless of their classification as benign or malignant [2,3,5]. Recent studies on brain tumors in Bangladesh indicate a daily increase in the number of persons afflicted by this condition. Sarkar et al. conducted a survey on the spectrum of brain tumors among patients at a tertiary care hospital in Bangladesh. The study was performed on 92 people.

The male-to-female ratio in this survey was 1.3:1, indicating a predominance of men. In addition to other brain cancers, the prevalence rates of astrocytic tu mors (42.50%), meningiomas (14.17%), oligodendrogliomas (10%), and embryonal tumors (7.50%) were significant in the analysis of the spectrum of brain tumors identified [6]. In a separate investigation, Rahman et al. examined 320 instances of brain tumors. The patients in this study ranged in age from 10 months to 75 years. The ratio of men to women is 2:1. Adults had 20% infra-tentorial tumors and 80% supra tentorial malignancies. Children constituted 29.8% of supratentorial tumors and 71.25% of infratentorial tumors. Additionally, each year, primary CNS malignancies result in the deaths of between 11,000 and 13,000 Americans [7]. Various techniques exist for detecting brain tumors. Clinical evaluation, imaging techniques, and biopsy are frequently employed. Clinical examinations involve a physical assessment by a healthcare practitioner to identify signs and symptoms of malignancies, including masses, alterations in skin color or texture, and abnormalities in organ function. Nonetheless, a basic clinical diagnosis is insufficient; a thorough examination of the body is essential [8]. X-rays, CT scans, and MRIs are used for tumor detection [9]. MRI is a superior method for identifying malignancies compared to other procedures. MRI has superior soft-tissue resolution compared to X-ray and CT scans, and it can acquire images in multiple planes (axial, coronal, and sagittal)[9]. Magnetic Resonance Imaging (MRI) enables the simultaneous visualization of the size, shape, and location of individual tumors from many perspectives. MRI is a non-invasive imaging modality that does not necessitate invasive tissue sampling, such as a biopsy, and does not subject individuals to ionizing radiation.

Artificial intelligence (AI), now a standard approach in medical diagnostics, is essential for identifying brain cancers. It demonstrates tools for generational segmentation. The conventional approach prevails in the first generation of brain lesion segmentation (BLS). Machine learning (ML) and deep learning (DL)-based artificial intelligence systems prevailed in the second and third generations [10–12]. The methodologies employed by machine learning and deep learn ing to extract properties from examples vary. Numerous machine learning (ML) classification models are developed as

independent analytical learning systems that yield precise predictions, contingent upon the data's attributes. Research has shown that machine learning enhances tissue characterization in medical imaging applications [12–14]. This research proposes a model utilizing deep learning and machine learning methods for the categorization and segmentation of brain tumor MRI data. Machine learning algorithms, including Support Vector Machines, K-Nearest Neighbors, and Random Forests, have been extensively used for tumor classification. They employ characteristics including texture, shape, intensity histograms, and frequency-domain descriptors [15,16]. These models are predominantly effective on smaller datasets, frequently depend on domain expertise for feature selection, and may exhibit limited generalizability. Conversely, deep learning models, including Convolutional Neural Networks and their advanced variants such as ResNet50, can learn hierarchical feature representations directly from raw MRI data, thereby enhancing classification accuracy across multiple imaging domains[9,12,17–21].

In tumor segmentation, U-Net has established itself as the benchmark architecture for precisely delineating tumor boundaries at the pixel level. U-Net employs an encoder-decoder architecture with skip connections to maintain spatial information and context across scales, a method initially introduced for biomedical segmentation tasks [22–24]. In scenarios with little labeled data, such as liver, lung, and brain tumor segmentation, it has demonstrated remarkable efficacy [25,26]. The performance of U-Net has been enhanced through modifications that include contextual attention and volumetric learning, such as the attention U-Net, ResU-Net, and 3D U-Net [27].

This study presents and assesses a hybrid framework for comprehensive brain tumor analysis using 2D MRI data that integrates machine learning (ML) and deep learning (DL) methodologies. We utilize ResNet50, SVM, KNN, and Random Forest classifiers to differentiate among glioma, meningioma, pituitary tumor, and non-tumor cases. We uti lize the U-Net architecture to delineate tumor regions from the input slices. We developed an end-to-end pipeline that combines U-Net-based segmentation with a Random Forest classifier to harness the advantages of both deep learning and traditional machine learning. This hybrid method facilitates precise tumor identification and subsequent classification uti lizing extracted region-specific information, with the objec tive of balancing performance, interpretability, and computing efficiency.

## 2. Related Works

The categorization of brain tumors employing both machine learning (ML) and deep learning (DL) techniques has been thoroughly investigated. Sharma et al. [28] presented a brain tumor detection method employing machine learning techniques. The suggested methodology consists of three stages: preprocessing of brain MRI images, extraction of texture features via the Gray Level Co-occurrence Matrix (GLCM), and classification of images via machine learning techniques. The classification of Brain MRI images was accomplished using a Multi-Layer Perceptron (MLP) and Naive Bayes, resulting in accuracies of 98.6% and 97.6%, respectively. Kshirsagar et al. [29] developed a machine learning system for detecting brain tumors using MRI data. The study used 212 instances of magnetic resonance images for data processing. The Multi-layer Perceptron and Naive Bayes algorithms attain accuracies of 98.6% and 91.6%, respectively. Siddique et al. [30] built a deep convolutional neural network model for brain tumor identification utilizing brain MRI images. A total of 253 brain MRI pictures were utilized, with 155 designated as malignancies. Their proposed model has an overall classification accuracy of 96%. Abdusalomov et al.[31] suggested a method for detecting brain tumors that employs MRI images to train a deep neural network. The research employed the YOLOv7 model to identify glioma, meningioma, and pituitary cancers. The model exhibits an overall accuracy of 99.5%. Sadad et al. [32] devised a methodology for brain tumor detection and multi-classification employing sophisticated deep learning techniques. The authors employed ResNet50, DenseNet201, MobileNet V2, and InceptionV3 deep learning techniques for multi-class classification in this work. Of these, NASNet exhibits the best accuracy at 99.6%.

Sajid et al.[33] devised a system for the detection and segmentation of brain tumors in MR images via deep learning algorithms. This study introduces a deep learning approach that employs various MRI modalities for brain tumor segmentation. They suggested a hybrid convolutional neural network architecture utilizing a patch-based approach to predict the output label, including both local and contextual information. The proposed method is validated with the BRATS 2013 dataset, showing enhancements over leading techniques, achieving dice scores, sensitivities, and specificities of 0.86, 0.91, and 0.86 for the entire tumor region. Jia and Chen suggested a method for the identification and categorization of brain tumors via deep learning techniques applied to MRI images[34]. This study introduces a completely automated heterogeneous segmentation method for brain tumor delineation, employing deep learning techniques and a support vector machine (FAHS-SVM). The quantitative results indicate the system's efficacy, achieving an accuracy of around 98.51% in distinguishing between sick and normal tissues in brain magnetic resonance imaging.

Methil and Aryan Sagar[35] introduced a technique for brain tumor identification via deep learning and image processing. This study employed a convolutional neural network (CNN) for classification purposes. CNN exhibited an impressive recall of 98.55% on the training set and 99.73% on the validation set. ResNet101v2 served as the foundational model for transfer learning, an alternative to pre-trained models. Subsequent training was conducted to enhance the task.

Numerous studies have investigated feature fusion and hybrid methodologies. Amin et al.[36] devised a methodology for the detection of brain cancers via feature fusion and machine learning approaches. They employed an unsupervised clustering methodology for tumor segmentation in their research. A fusion of Gabor wavelet features (GWF), local binary patterns (LBP), histograms of oriented gradients (HOG), and segmentation-based fractal texture analysis (SFTA) characteristics is employed to construct a composite feature vector. A Random Forest classifier was used to classify tumor types. Mathiyalagan et al.[37] proposed a machine learning method for the classification of glioma brain tumors. This study employed a ridgelet filter to identify and eliminate noise from the original brain MRI image. Fuzzy logic is employed to identify edges in the noise-reduced image, followed by contrast-adaptive local histogram equalization to enhance the edge pixels of the edge-detected brain image. The enhanced brain image undergoes a Gabor transformation, and characteristics are retrieved from the resultant image. The genetic algorithm (GA) optimizes the computed features. The refined features are further categorized utilizing the adaptive neuro-fuzzy inference system (ANFIS) classification approach, which segregates the source brain MRI image into two classifications: pictures with gliomas and images without gliomas.

In the context of segmentation, U-Net remains the predominant design for medical imaging. Despite a limited dataset, the model's encoder-decoder architecture with skip connections facilitates dependable border identification. For intricate segmentation jobs, we currently possess variations such as U-Net++, Attention U-Net [38], and 3D U- Net [39], which have enhanced performance. The BraTS challenge[40] has been utilized as a standard specifically for brain tumor segmentation. It advocates for architectures capable of multi-modal MRI analysis and multi-class tumor classification.

Despite considerable advancements in tumor analysis, the majority of current research emphasizes on classification or segmentation, rather than integrating both methodologies. Limited methodologies provide a cohesive solution that addresses both responsibilities within a singular framework. Furthermore, while 3D deep learning models frequently attain great accuracy, they are resource-intensive and generally necessitate substantial data and robust technology. We mitigate these constraints by employing machine learning and deep learning classifiers, namely ResNet50, SVM, Random Forest, and KNN, for tumor type classification. We employ the U-Net architecture for

segmentation to delineate tumor areas at the pixel level from 2D MRI slices. This hybrid technique facilitates dependable classification and precise geographical localization while preserving a comparatively cheap computational expense. This is particularly crucial in environments with restricted data or hardware limitations.

## 3. Methodology: The Twin-View Framework

A literature study indicated that automated brain tumor diagnosis is essential due to its implications for human life and the necessity for high precision. Tumors can be autonomously identified in magnetic resonance imaging by the application of machine learning and deep learning algorithms for feature extraction, classification, and segmentation. This work presents the development of an automated system utilizing machine learning and deep learning techniques for the precise classification and segmentation of brain tumors.

### A. Data Collection

Extensive image datasets are essential for machine learning training. While numerous databases are accessible to researchers, additional resources are required. Public platforms like Kaggle provide an extensive array of annotated medical imaging datasets, rendering them a significant resource for the development and validation of machine learning models. The dataset comprises 7,023 pictures [41]. They are categorized into four classes.

- Glioma
- Meningioma
- Pituitary Tumor
- Non-Tumor

Each image possesses a resolution of 256 by 256 pixels and is stored in JPEG format. The OpenCV Python library is utilized to transform all photos into designated shapes. Fig 1. illustrates the entire quantity of photos inside each class of the dataset whereas Fig. 2 displays the initial image of each class in both the test and training sets.

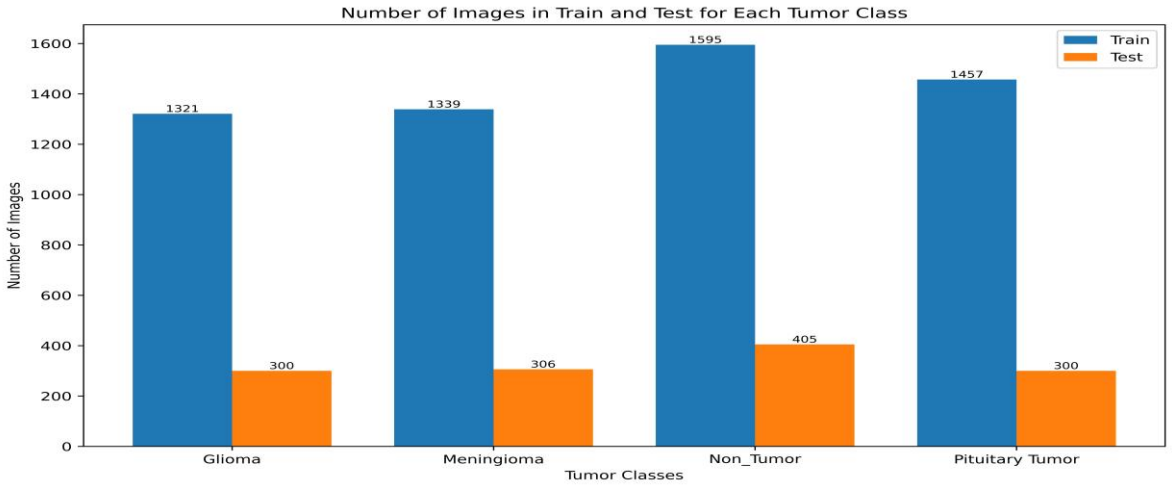


Fig. 1: Dataset profile: Total sample and class distribution.

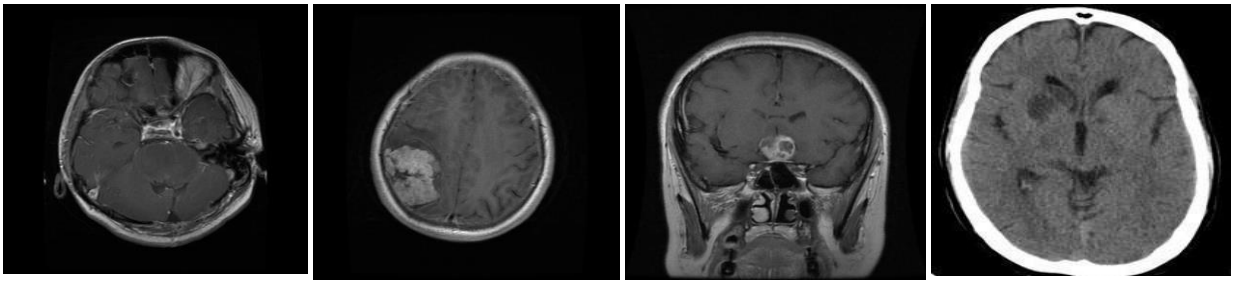

(a) (b) (c) (d)

Fig. 2: Multi-modal neuroimaging samples across dataset classes: (a)–(c) Contrast-enhanced MRI slices showcasing glioma, meningioma, and pituitary tumors respectively, and (d) non-tumor CT scan.

**B. Textural Characteristics of the Dataset**

Texture features are quantitative metrics or descriptors that encapsulate diverse characteristics of texture patterns in a picture. These features are derived from the spatial distribution of pixel intensity values and are utilized to define the visual characteristics, structure, and qualities of textures within the image. Standard texturing features comprise:

- Gray Level Co-occurrence Matrix (GLCM),
- Local Binary Patterns (LBP),
- Gabor Filters,
- Mask.

**Gray Level Co-occurrence Matrix (GLCM):** Fig. 3 illustrates the GLCM textural characteristics of an image inside the collection. The Gray Level Co-occurrence Matrix is a statistical technique employed for texture analysis in digital imagery. It delineates the spatial relationships among pixel intensity values in a picture and estimates the frequency of certain intensity value pairs at designated spatial relationships. Elevated contrast levels signify that the intensity values inside the image fluctuate swiftly across adjacent pixels, producing pronounced transitions or edges. Low contrast levels signify that the intensity values in the image either vary gradually or remain stable.

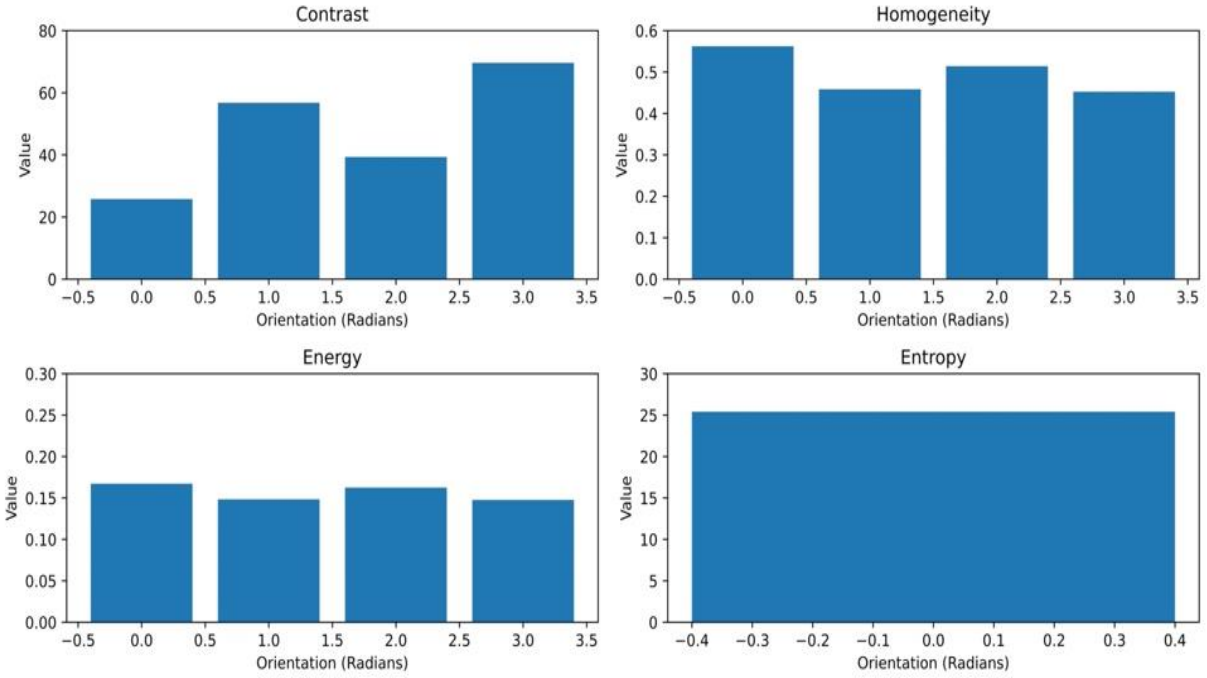


Fig. 3: GLCM texture descriptors as a function of orientation: Variations in contrast, homogeneity, energy, and entropy derived from a sample neuroimage across four directional angles (in radians).

**Local Binary Patterns (LBP):** It is a texture descriptor that encapsulates local variations in pixel intensity. It measures the local association between a pixel and its adjacent pixels by recording the binary patterns generated from comparing the intensity values of the pixel with those of its neighbors.

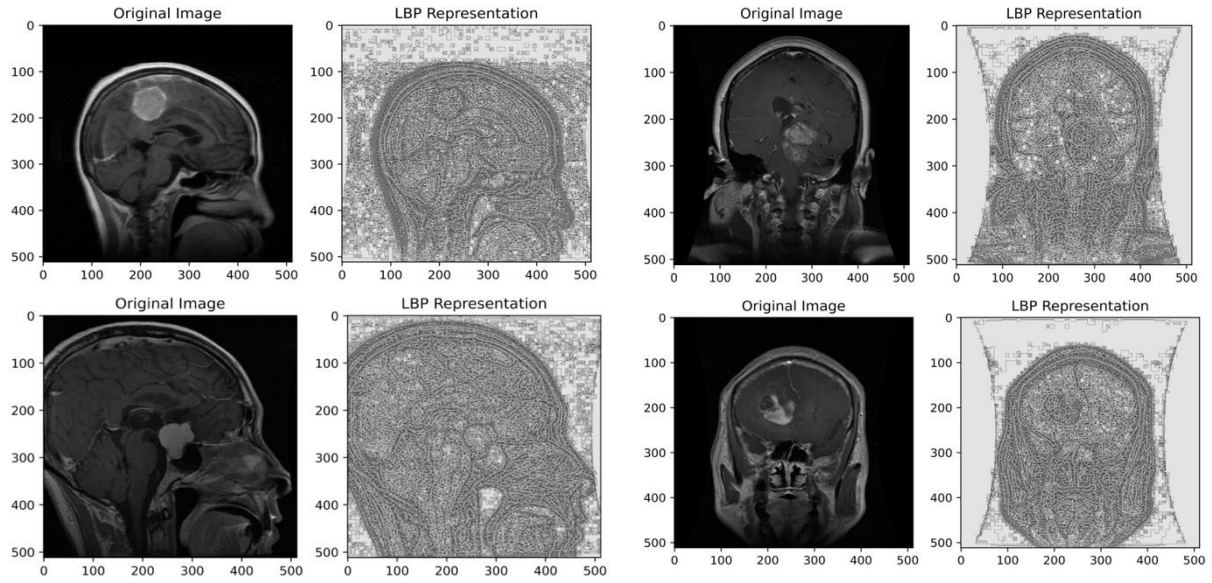


Fig. 4: Local Binary Pattern (LBP) texture extraction on representative brain scans: Comparison between original multi-view MRI slices (left panels) and their corresponding LBP feature representations (right panels), demonstrating localized surface texture variation in tumor regions

The LBP representation elucidates the texture patterns inherent in the image. Dark colors signify regions with analogous texture patterns, whilst lighter parts suggest greater variability in texture patterns. Fig. 4 illustrates the LBP representation of tumor brain images, while Fig. 5 depicts the LBP representation of non-neoplastic images.

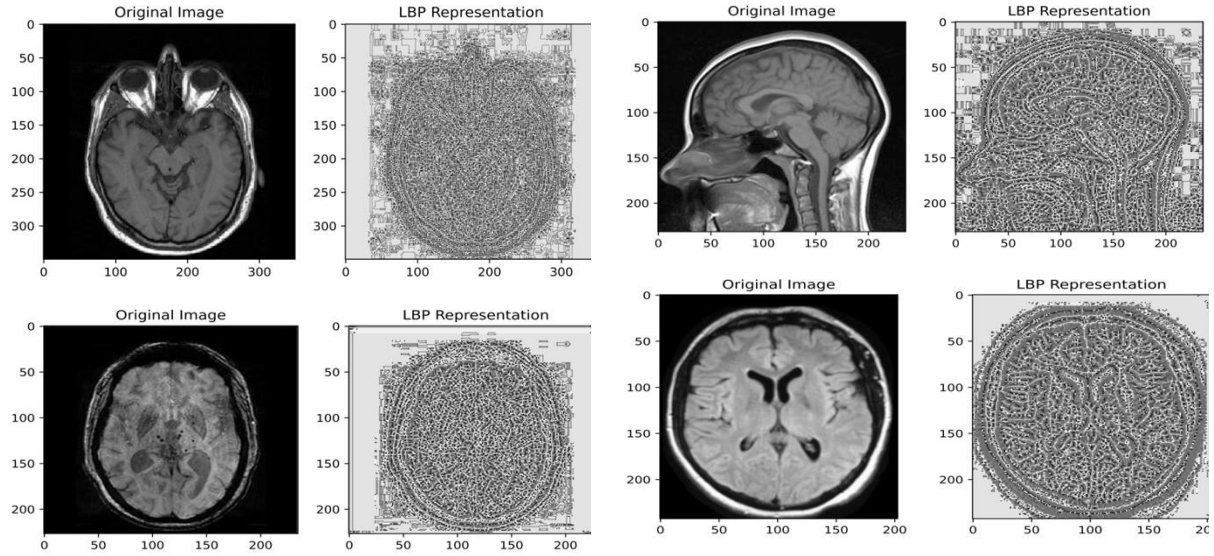


Fig. 5: Local Binary Pattern (LBP) feature maps for non-neoplastic control samples: Side-by-side comparison of original structural brain MRI slices and their corresponding LBP feature representations, highlighting the baseline micro-texture distribution of healthy tissue.

The LBP procedure for feature extraction was implemented on the gray-level MRI slices of all tumor classifications. The photos were downsized to a consistent resolution of 128x128 pixels and converted to grayscale if not previously completed. LBP patterns were derived with a circular neighborhood of 8 sample points with a radius of 1 pixel to ensure rotational invariance. The LBP-encoded images were subsequently utilized to calculate the histogram of LBP values, serving as compact feature vectors for machine learning classifiers including SVM, KNN, and Random Forest.

**Gabor Filter:** Orientation-sensitive texture characteristics from brain MRI images were recovered utilizing Gabor filters. Gabor filters effectively emulate the responses of the human visual system to spatial frequencies and orientations, making them adept in detecting local structures such as edges and ridges. A Gabor filter integrates a Gaussian envelope with a sinusoidal carrier, enabling the simultaneous recording of spatial and frequency information.

The subsequent equation delineates the intricate representation of the Gabor filter Eq. (1):

$$G(x, y; \lambda, \theta, \psi, \sigma, \gamma) = exp\left(-\frac{x'^2+\gamma^2 y'^2}{2\sigma^2}\right) cos\left(\frac{2\pi x'}{\lambda} + \psi\right) \qquad (1)$$

Here $\lambda, \theta, \psi, \sigma, \gamma$ is the response of the Gabor filter at pixel location (x,y). They are the spatial coordinates. $\lambda$ is the wavelength of the sinusoidal component of the Gabor function, $\theta$ represents normal's orientation to the Gabor function's parallel stripes, $\psi$ is the phase offset, $\sigma$ specifies the standard deviation of the Gaussian envelope, and $\gamma$ accounts for the spatial aspect ratio, for the ellipticity of the support of the Gabor function.

This model employs a bank of Gabor filters at four orientations (0°, 45°, 90°, and 135°) for each gray-scale MRI slice. Distinct output images are generated from each Gabor response, resulting in diverse directional patterns applied to images, hence enhancing edge and structural differences, particularly in tumor regions. Statistical features, including the mean, variance, and energy, are calculated for each Gabor response, resulting in a descriptive feature vector. Fig. 6 shows the response of this filter on an original MRI image.

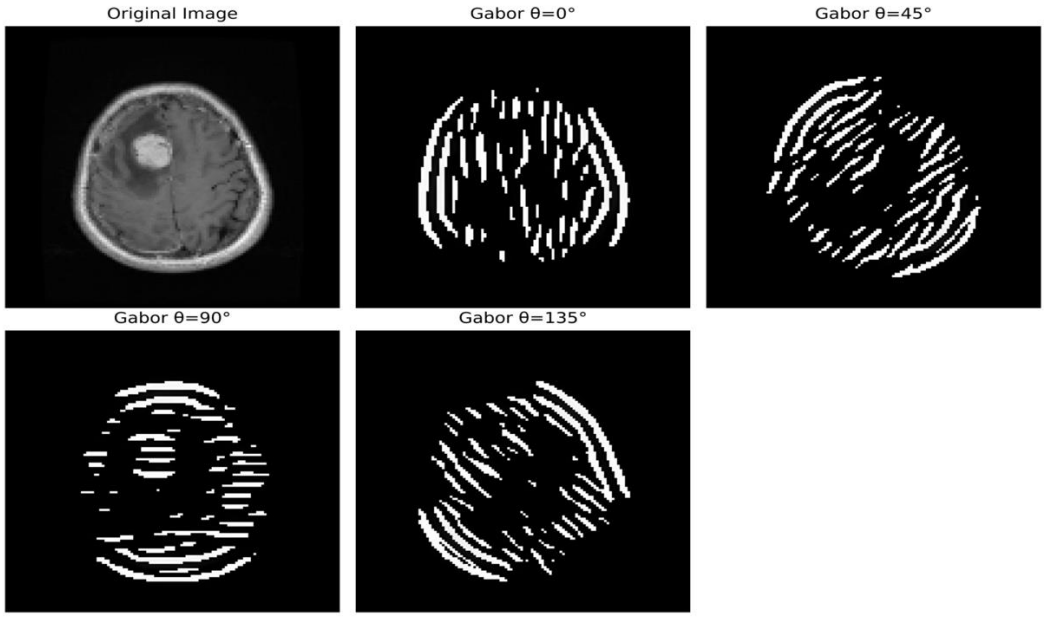


Fig. 6: Texture and edge enhancement via directional Gabor filters: Visual demonstration of convolving a baseline neuroimage with filter kernels at distinct orientations to extract orientation-sensitive pathological patterns.

**Binary Mask:** Binary tumor masks served as the ground truth annotations in the segmentation pipeline. Masks are two-dimensional binary pictures in which 1 denotes the tumor and 0 signifies the non-tumor backdrop. The masks are either pre-labeled or manually subdivided and utilized to supervise the training of the U-Net model. Binary masks, spatially anchored to the tumor structure, enable the model to acquire pixel-wise correspondences between raw MRI images and tumor regions. During training, the model optimizes a loss function (binary cross-entropy or Dice loss) between the anticipated mask and the ground truth (depicted in grey), facilitating precise border identification and tumor localization. Fig. 7 presents an illustration of brain MRI scans accompanied by their respective binary mask.

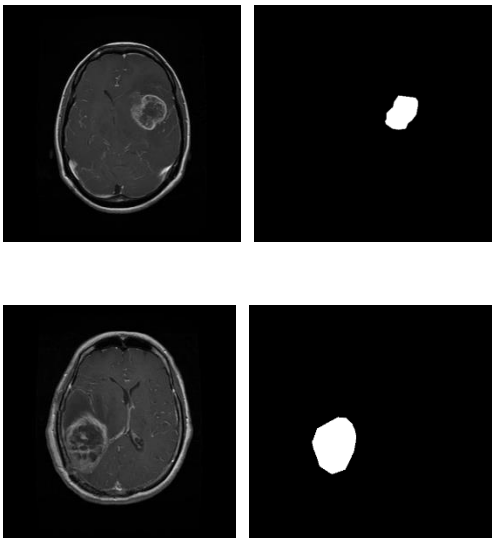

Fig. 7: Comparison of original MRI slices and matching binary segmentation masks for tumor localization.

**Performance Metrics (Dice Coefficient and IoU:** To quantitatively evaluate the performance of the U-Net segmentation model, we presented two widely utilized metrics in medical picture segmentation: the Dice Similarity Coefficient (DSC) and Intersection over Union (IoU). The Dice coefficient quantifies the intersection between the anticipated segmentation mask and the ground truth mask, defined as Eq. (2):

$$Dice = \frac{2|A \cap B|}{|A|+|B|} \quad (2)$$

In this context, A and B denote the sets of expected and actual tumor pixels, respectively; a Dice score of 1 signifies complete overlap, whereas a score of 0 implies no overlap.

The Intersection over Union (IoU), sometimes referred to as the Jaccard Index, is defined as follows Eq. (3):

$$IoU = \frac{|A \cap B|}{|A \cup B|} \quad (3)$$

This metric is more conservative than the Dice coefficient and assesses the extent of overlap between the anticipated mask and the annotated tumor region. Both were observed during training to assess model convergence and generalization.

### C. Brain Tumor Classification Framework

This research employs deep learning and three machine learning models to compare their performance with the test data and to find which algorithm works better with three distinct tumor categories and one non-tumor category.

**Resnet-50:** We have developed a ResNet50 model for the classification of brain tumor pictures, utilizing the robust capabilities of residual networks to attain enhanced performance. The architecture of our ResNet50 model is engineered to classify complex aspects within photos represented in Fig.8.

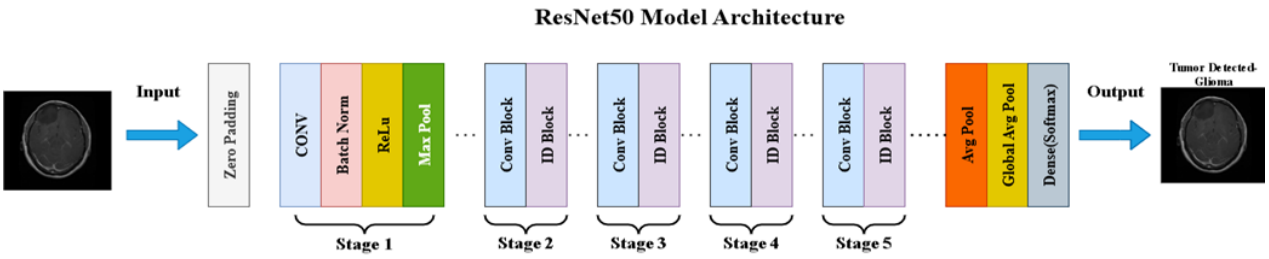


Fig. 8: ResNet-50 Modified Architecture

We employed a modified ResNet50 architecture to classify brain cancers utilizing grayscale magnetic resonance imaging (MRI) images downsized to $100 \times 100$ pixels. The model was engineered to accept input tensors with

dimensions $100 \times 100 \times 1$, representing single-channel grayscale images. To modify the conventional ResNet50 for our reduced input dimensions and decrease model complexity, we substituted the final Flatten operation with a Global Average Pooling2D layer, which mitigates overfitting by consolidating spatial features. The architecture consists of a primary convolution layer featuring a $7 \times 7$ kernel and a stride of 2, succeeded by batch normalization, ReLU activation, and max pooling. A sequence of convolutional and identity residual blocks is implemented, structured into five stages, with progressively increasing filter dimensions of [64, 128, 256, 512]. The residual learning framework incorporates skip connections, whereby the output of a residual block is defined as Eq. (4):

$$y = F(x, W_i) + x \quad (4)$$

Here, $x$ is the input tensor, $F(x, \{W_i\})$ represents the stacked convolution–batchnorm–ReLU operations with weights $\{W_i\}$, and the addition corresponds to the identity shortcut.

Each convolutional layer in the network performs the operation Eq. (5):

$$Conv(x) = (x * W) + b \quad (5)$$

Where, $x$ is the input feature map, $W$ the convolution kernel, $b$ the bias, and $*$ denotes the convolution operation. Following each convolution, batch normalization is applied Eq. (6):

$$BN(z) = \gamma \frac{z-\mu}{\sqrt{\sigma^2+\epsilon}} + \beta \quad (6)$$

where $z$ is the activation, $\mu$ and $\sigma^2$ are the mean and variance of the batch, and $\gamma$, $\beta$ are learned scale and shift parameters. ReLU activation is applied as Eq. (7):

$$ReLU(x) = max(0, x) \quad (7)$$

After the final convolutional stage, Global Average Pooling2D is applied to reduce each feature map to a scalar by averaging all spatial elements Eq. (8):

$$y_k = \frac{1}{H \times W} \sum_{i=1}^{H} \sum_{j=1}^{W} x_{ijk} \quad (8)$$

Where $x_{ijk}$ is the value at position $(i, j)$ in channel $k$, and $H$, $W$ are the height and width of the feature map.

The pooled features are passed to a fully connected softmax layer for classification Eq. (9):

$$\hat{y}_i = \frac{exp(z_i)}{\sum_{j=1}^{C} exp(z_j)} \quad (9)$$

Where $\hat{y}_i$ is the predicted probability of class $i$, $z_i$ is the logit (input to softmax), and $C$ is the number of tumor classes (in this case the value is 4).

To enhance convergence and generalization, we utilized the Adam optimizer with a specified learning rate. All layers and parameters were started with default TensorFlow initializers, and the model was trained for 30 epochs with a batch size of 32. Table.1 describes the ResNet50 blocks.

Table 1: Layer-by-layer architectural breakdown and output shape transformations of the proposed ResNet-50 classifier

| Stage | Layer Type | Kernel / Stride | Output Shape | Blocks | Operation |
|---|---|---|---|---|---|
| Input | Input | - | 100 × 100 × 1 | - | Grayscale MRI Image |
| Conv1 | Conv2D + BatchNorm + ReLU | 7 × 7, stride 2 | 47 × 47 × 64 | 1 | Initial feature extraction |
| Conv2_x | Max Pooling | 3 × 3, stride 2 | 23 × 23 × 64 | 1 | Spatial down-sampling |
| Conv2_x | Residual Block | 1 × 1, 3 × 3, 1 × 1 | 23 × 23 × 256 | 3 | Feature learning with identity mapping |
| Conv3_x | Residual Block | 1 × 1, 3 × 3, 1 × 1 | 12 × 12 × 512 | 4 | Deeper feature extraction |
| Conv4_x | Residual Block | 1 × 1, 3 × 3, 1 × 1 | 12 × 12 × 1024 | 6 | High-level feature representation |
| Conv5_x | Residual Block | 1 × 1, 3 × 3, 1 × 1 | 12 × 12 × 2048 | 3 | Semantic feature extraction |
| Output | Global Average Pooling + Dense + Softmax | - | 4 | 1 | Four-class brain tumor classification |

**Random Forest**: The Random Forest model, an ensemble learning technique, constructs many decision trees during training to obtain the class that signifies the mean prediction (regression) or the mode of the classes (classification) for each tree. Features are extracted from images utilizing the Histogram of Oriented Gradients (HOG) approach during the feature extraction procedure. HOG descriptors include the distribution of local gradient orientations inside a picture, hence conveying information regarding object forms and textures. The extraction of HOG features occurs in multiple stages:

Gradient Calculation: The gradient components in the x and y directions are determined as follows Eq. (10):

$$\frac{\partial G}{\partial x} = \frac{\partial I}{\partial x'}$$

$$\frac{\partial G}{\partial y} = \frac{\partial I}{\partial y} \quad (10)$$

The gradient magnitude M is calculated as the square root of the sum of the squares of the gradients in the $x$ and y axes. This magnitude denotes the comprehensive intensity of the gradient at every pixel. The gradient orientation $\theta$ is calculated as the arctangent of the ratio of the y-gradient to the x-gradient. It denotes the direction of the fastest intensity variation.

The gradient magnitude M and orientation $\theta$ are computed as Eq. (11):

$$M = \sqrt{G_x^2 + G_y^2}$$

$$\theta = arctan\left(\frac{G_x}{G_y}\right) \quad (11)$$

Normalization often entails dividing the histogram by a factor obtained from the histogram values inside a certain block Eq. (12).

$$v = \frac{1}{|H|^2 + \epsilon} \quad (12)$$

In this context, $\epsilon$ represents a negligible constant to prevent division by zero.

The random forest classifier computes decision trees, Gini impurity, and entropy. Decision trees within a Random Forest are generally depicted as a sequence of if-else statements that partition the feature space according to specific criteria. At every internal node t, a decision is rendered based on the feature $x_i$ and the threshold $\theta$. If $x_i$ is less than or equal to $\theta$, proceed to the left child; otherwise, proceed to the right child. The decision tree systematically

divides the feature space until predetermined halting criteria are satisfied. Gini impurity quantifies node impurity in decision trees Eq. (13).

$$G(t) = 1 - \sum_{i=1}^{C} p\,(i|t)^2 \quad (13)$$

where $C$ is the number of classes and $p(i \mid t)$ is the proportion of samples of class $i$ at node $t$. Entropy is another measure of node impurity Eq. (14).

$$H(t) = -\sum_{i=1}^{C} p\,(i|t)\,log_2(p(i|t))) \quad (14)$$

Like Gini impurity, lower entropy indicates higher purity.

**Support Vector Machine:** The SVM model is a supervised learning method employed for classification purposes. It functions by identifying the optimal hyperplane in the feature space to segregate several classes. For brain tumor classification, the SVM model is trained using a collection of labeled images, with each image represented by a feature vector derived from the image data. Features are generally retrieved via approaches such as Histogram of Oriented Gradients (HOG), which encapsulates the shape and texture information of images. Upon training, the SVM model is capable of categorizing novel brain tumor images into distinct classes according to their extracted attributes. The essential elements of the Support Vector Machine employed in classification are:

Decision Function: The decision function in SVM calculates the sign of a linear combination of input characteristics weighted by Lagrange multipliers, incorporating a bias term. This function identifies the class boundary or hyperplane that distinguishes various classes inside the feature space Eq. (15).

$$f(x) = sign(\sum_{i=1}^{N} \alpha_i\, y_i K(x_i, x) + b) \quad (15)$$

In this context, $x_i$ represents the training samples, $y_i$ denotes the associated class labels, $\alpha_i$ signifies the Lagrange multipliers, and b refers to the bias term. $K(x_i, x)$ is the kernel function that calculates the inner product between $x_i$ and $x$.

Kernel Function: The kernel function is a technique employed to map input data into a higher-dimensional space, enabling the Support Vector Machine (SVM) to identify a hyperplane that distinguishes the data when a linear boundary is absent in the original feature space. It calculates the inner product between pairs of input data points within this elevated-dimensional space. The kernel functions employed for brain image categorization are Eq.(16), (17), (18):

Linear Kernel:

$$K(x_i, x) = x_i^T x \quad (16)$$

Polynomial Kernel:

$$K(x_i, x) = (x_i^T x + c)^d \quad (17)$$

Radial Basis Function (RBF) Kernel:

$$K(x_i, x) = exp(-\gamma |x_i - x|^2) \quad (18)$$

Optimization: The optimization method in SVM entails identifying the best hyperplane that increases the margin between distinct classes while minimizing classification errors.

This is accomplished by resolving a convex optimization problem, generally structured as a quadratic programming (QP) problem, where the objective is to minimize a loss function Eq. (19).

$$\min_{\alpha} \left[\frac{1}{2} \sum_{i=1}^{N} \sum_{j=1}^{N} \alpha_i\, \alpha_j y_i y_j K(x_i, x_j) - \sum_{i=1}^{N} \alpha_i\right] \quad (19)$$

Subject to the constraint Eq. (20):

$$0 \le \alpha_i \le C, \qquad \sum_{i=1}^{N} \alpha_i y_i = 0 \tag{20}$$

Here, $\alpha_i$ are the Lagrange multipliers, $C$ is the regularization parameter controlling the trade-off between maximizing the margin and minimizing the classification error, $y_i$ are the class labels. The SVM model is trained by solving this optimization.

**KNN**: It is a non-parametric, slow learning method employed for classification and regression tasks. It retains all existing cases and categorizes new cases according to a similarity metric (e.g., distance functions like Euclidean distance). The Euclidean distance formula is frequently employed as the distance metric in KNN Eq. (21):

$$d(x, y) = \sqrt{\sum_{i=1}^{n} (x_i - y_i)^2} \tag{21}$$

Here, $x$ and $y$ are two data points in n-dimensional space. $x_i$ and $y_i$ are the i-th features of data points $x$ and $y$, respectively. The algorithm selects the k nearest neighbors of a given data point x based on the computed distances. It then assigns the majority class label among these k neighbors to the data point $x$. After identifying the k nearest neighbors, the algorithm determines the class label for the new data point by selecting the label that appears most frequently among the k neighbors.

LBP encodes texture by applying thresholding to the local neighborhood of each pixel. A binary code is generated for each pixel by comparing it with its neighboring pixels using Eq. (22):

$$LBP(x_c, y_c) = \sum_{p=0}^{P-1} s\left(g_p - g_c\right) \cdot 2^p \tag{22}$$

where $g_c$ is the center pixel and $g_p$ are the neighboring pixels. We employed uniform patterns with $P = 24$ and $R = 3$, yielding 26 histogram bins. LBP detects nuanced differences in brain texture that are frequently imperceptible to the naked eye.

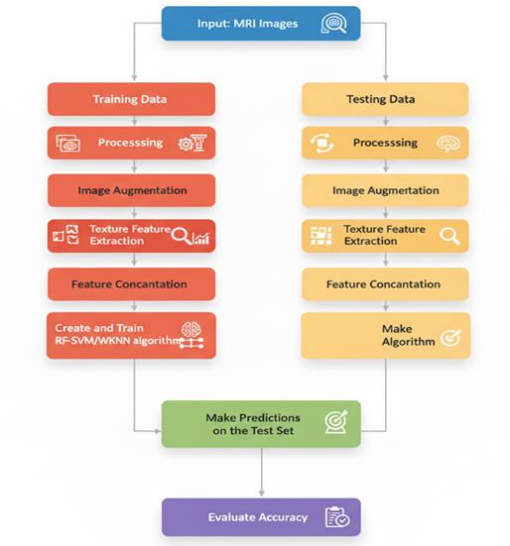


Fig. 9: Schematic overview of the proposed classification framework from raw MRI input to performance evaluation.

Fig. 9 depicts the architecture of machine learning models, specifically Random Forest, Support Vector Machine (SVM), and K-Nearest Neighbors (KNN).

**D. Segmentation Model**

We employed a U-Net architecture for the pixel-wise segmentation of brain tumors in grayscale MRI slices. U-Net is a symmetrical architecture with an encoder-decoder convolutional neural network (CNN) specifically developed for biomedical picture segmentation. The network received a preprocessed $128 \times 128$ grayscale MRI image along with binary masks representing identified tumor areas. The encoder path (contraction path) progressively acquires contextual features via a sequence of two $3 \times 3$ convolutional layers (including ReLU activation and appropriate padding) and $2 \times 2$ max pooling. The quantity of filters doubles at each down-sampling stage, commencing at 64 and reaching 1024 throughout five levels of resolution. The decoder path, akin to the encoder, comprises up-sampling via $2 \times 2$transposed convolutions, succeeded by two $3 \times 3$ convolutions, and concatenation with the corresponding encoder layer using skip connections. This integration preserves the spatial continuity and edge information essential for effective segmentation. The final output layer consists of a$1 \times 1$ convolution with a sigmoid activation function to generate a binary segmentation mask.

The model was constructed utilizing the Adam optimizer with a learning rate of 0.0001 and trained for 20 epochs with a batch size of 16. The employed loss function was binary cross-entropy, articulated as Eq. (23):

$$L_{BCE} = -\frac{1}{N}\sum_{i=1}^{N}[y_i\, log(\hat{y}_i) + (1 - y_i)\, log(1 - \hat{y}_i)] \qquad (23)$$

where $y_i$ is the true binary mask level and $\hat{y}_i$ is the predicted probability at pixel i. evaluates segmentation performance, we incorporated two custom metrics: the Dice coefficient and the Intersection over Union (IoU).

Table 2 illustrates the design of the U-Net model.

Table 2: Architectural details and feature map dimensions of the proposed U-Net model.

| Stage | Layer(s) | Kernel | Output Shape | Description |
|---|---|---|---|---|
| Input | Input Layer | - | (128,128,1) | Raw grayscale MRI image |
| Encoder Block 1 | 2× Conv2D + MaxPool | 3×3, ReLU | (128,128,64) | Low-level feature extraction |
| Encoder Block 2 | 2× Conv2D + MaxPool | 3×3, ReLU | (64,64,128) | MRI tissue representation and edge detection |
| Encoder Block 3 | 2× Conv2D + MaxPool | 3×3, ReLU | (32,32,256) | Capturing deeper contextual features |
| Encoder Block 4 | 2× Conv2D + MaxPool | 3×3, ReLU | (16,16,512) | Encoding high-level semantic features |
| Bottleneck | 2× Conv2D | 3×3, ReLU | (8,8,1024) | Bridge between encoder and decoder |
| Decoder Block 1 | UpSampling + Conv2D | 2×2, 3×3 | (16,16,512) | Upsampling and feature restoration |
| Decoder Block 2 | UpSampling + Conv2D | 2×2, 3×3 | (32,32,256) | Recovering spatial information |
| Decoder Block 3 | UpSampling + Conv2D | 2×2, 3×3 | (64,64,128) | Refining tumor boundary representation |
| Decoder Block 4 | UpSampling + Conv2D | 2×2, 3×3 | (128,128,64) | Producing fine segmentation maps |
| Output | Conv2D (Sigmoid) | 1×1 | (128,128,1) | Final binary segmentation mask |

### E. Adaptive Segmentation via Otsu's Method

Even though the output of the U-Net is an accurate probability maps, the transition from continuous values to a binary mask depends on an efficient threshold-based approach to allow contour extraction. Fixed threshold strategies are usually not very effective when dealing with intensity changes across multi-center MRI data. Therefore, in order to perform adaptive segmentation, Otsu's thresholding approach was used.

Otsu's thresholding is based on finding the best possible threshold which will minimize the intra-class variance $\sigma_B^2(k)$:

$$\sigma_B^2(k) = \omega_0(k)\omega_1(k)[\mu_0(k) - \mu_1(k)]^2 \qquad (24)$$

where $\omega_0$ and $\omega_1$ represent the probabilities of the two classes separated by a threshold $k$, and $\mu_0$ and $\mu_1$ denote their respective mean intensities. Since the thresholding is performed on an individual level for each image slice, the obtained segmentation mask corresponds to the specific distribution of intensity of each MRI image. As a result, reliable tumor localization is achieved, removing background noise and preserving the geometry of the region under consideration and creating a proper Region of Interest (ROI).

### F. Proposed "Twin-View" Brain Analyzer Model

Fig. 10 presents the proposed 'Twin-View' architectural design depicting a hybrid framework for brain tumor analysis that combines segmentation and classification. Despite the ResNet50 model attaining superior standalone accuracy (94%) in image classification, we incorporated a Random Forest classifier (90% accuracy) into our hybrid pipeline owing to its compatibility with structured features derived from U-Net segmentation output, expedited inference, and enhanced interpretability Table 3. The procedure commences with the entry of a 2D MRI image. The image is concurrently processed through two pathways: one for segmentation utilizing the U-Net model, which produces a binary tumor mask, and the other for classification employing Random Forest, where textural features such as HOG and LBP are retrieved to ascertain tumor kind. If the model predicts "Non-Tumor," the pipeline concludes after the labeling process. For tumor-positive predictions, the binary mask is analyzed to delineate contours that define tumor boundaries. The contours are filtered to remove noise. Upon the identification of valid contours, they are superimposed on the original picture alongside the anticipated tumor classification, yielding a visual representation of both tumor localization and categorization. The Twin-View model utilizes adaptive thresholding methods such as Otsu's algorithm to convert the probability map into a binary mask, defined as a decision function where pixels exceeding the threshold are classified as tumor regions and others as background. This cohesive method improves diagnostic precision and clarity in brain tumor identification.

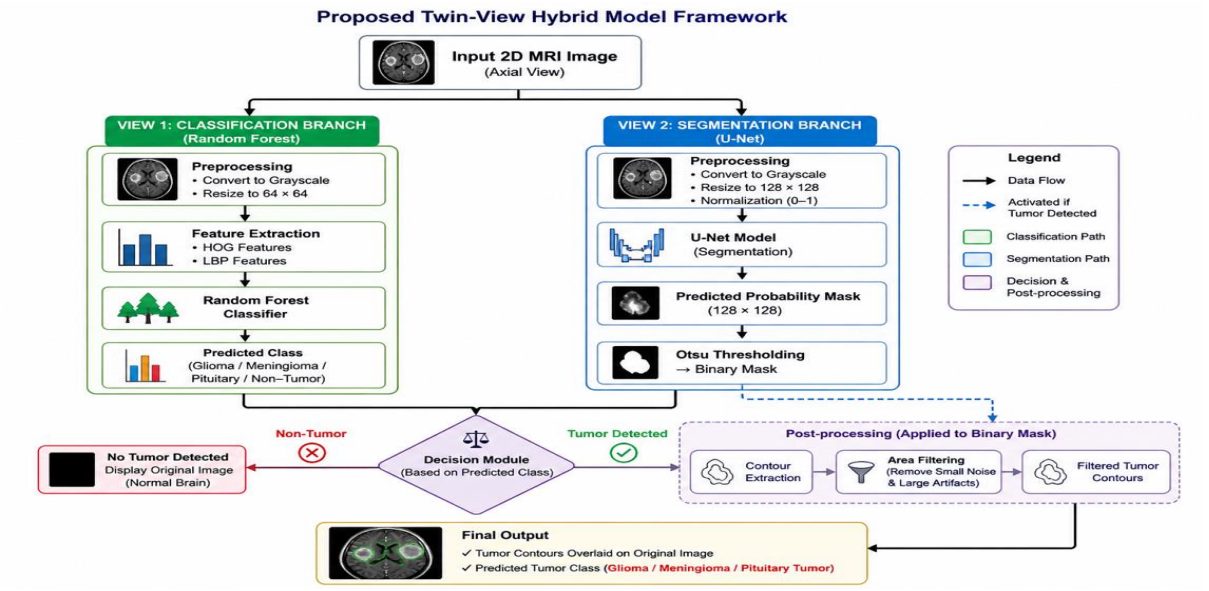


Fig. 10: Operational workflow of the proposed multi-task Twin-View hybrid model for concurrent brain tumor categorization and pixel-level delineation.

## IV. Experimental Results and Comparative Analysis

This section presents a comprehensive analysis and discussion of the experimental results obtained from the "Twin-View" hybrid framework for brain tumor analysis. The primary objective is to evaluate the performance of the proposed models for both tumor classification and segmentation. We begin by detailing the performance metrics used for quantitative assessment of the deep learning and machine learning models, including accuracy, precision, recall, and F1-score for classification, and the Dice coefficient and Intersection over Union (IoU) for segmentation. Subsequently, we present the confusion matrices and learning curves to illustrate the performance and training behavior of each model. A comparative analysis of our results with existing methodologies is also provided to highlight the contributions of this study. The discussion concludes with an examination of the hybrid model's effectiveness in providing both a classification label and a visual segmentation of the tumor. The Confusion Matrices of our proposed models are illustrated in Fig. 11 to 14.

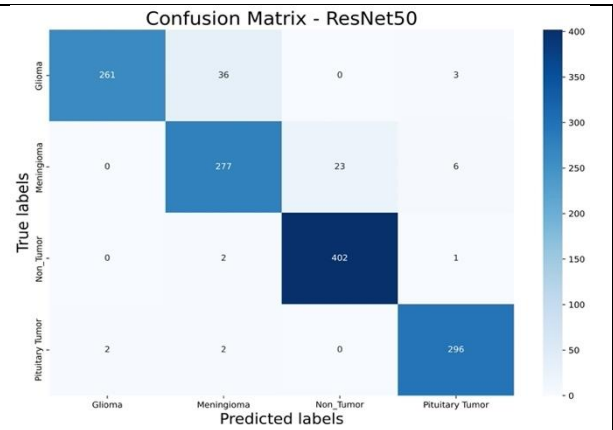


Fig. 11: Confusion Matrix of ResNet50

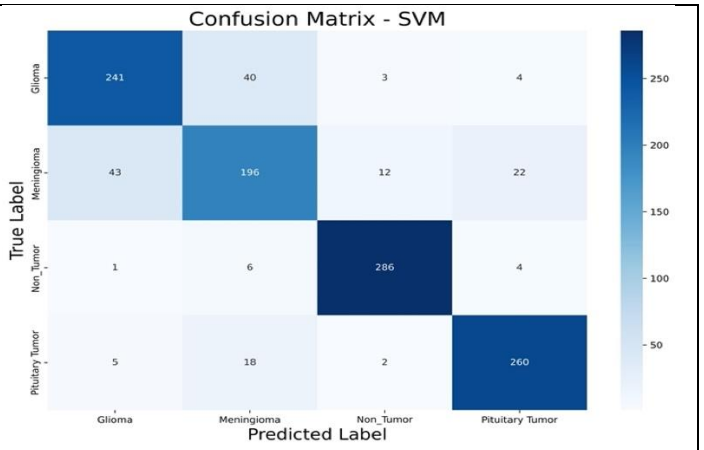


Fig. 12: Confusion Matrix of SVM

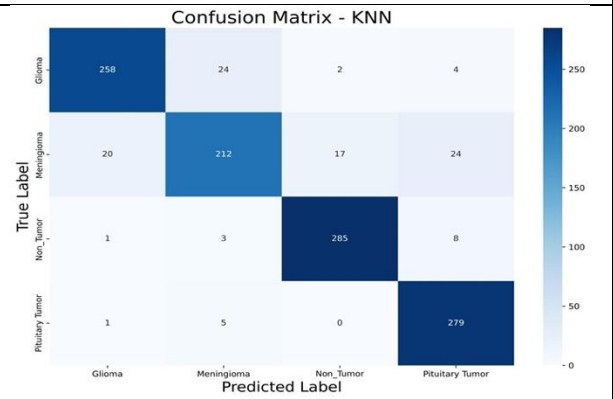


Fig. 13: Confusion Matrix of KNN

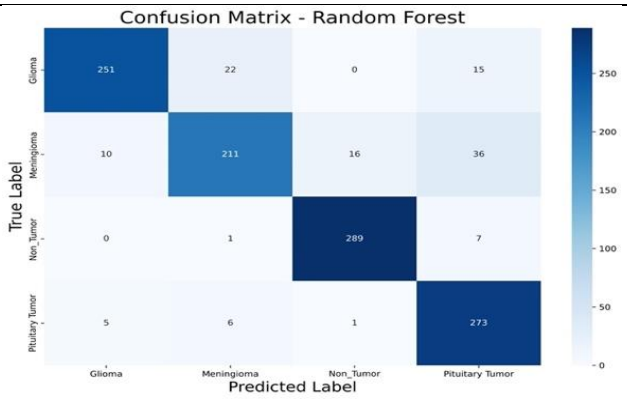


Fig. 14: Confusion Matrix of Random Forest

### A. Performance Evaluation Metrics

Performance evaluation measures are essential for evaluating the efficacy of models across many domains. These measures assess accuracy, precision, recall, and F1 score, offering insights into categorization or predictive capabilities. Accuracy evaluates overall correctness, precision reflects the model's ability to minimize false positives, recall measures its effectiveness in identifying all pertinent instances, and the F1 score reconciles precision and recall. This research presents a model of 7023 brain MRI scans. Our methodology is designed for multiclass categorization, encompassing four distinct classes. The confusion matrix has dimensions of $[4 \times 4]$ and can be expressed as Eq. (25):

$$\begin{bmatrix} TP_1 & FN_{12} & FN_{13} & FN_{14} \\ FP_{21} & TP_2 & FN_{23} & FN_{24} \\ FP_{31} & FP_{32} & TP_3 & FN_{34} \\ FP_{41} & FP_{42} & FP_{43} & TP_4 \end{bmatrix} \quad (25)$$

The TNs are not immediately displayed in the matrix as they are distributed over the complimentary locations.

Let $a_{ij}$ be the element in the row $i$, column $j$ of the confusion matrix, where:

$i$ is the true class and $j$ is the predicted class. $k$ is the targeted class.

Let,

$TP_k = a_{kk}$, $FP_k = \sum_{i \neq k} a_{ik}$, $FN_k = \sum_{j \neq k} a_{kj}$

$TN_k = \sum_{i \neq k} \sum_{j \neq k} a_{ij,}$ (i.e., all values not in row $k$ or column $k$)

For our model, the overall accuracy can be calculated by the following metrics:

$$\text{Accuracy} = \frac{\sum_{k=1}^{4} a_{kk}}{\sum_{i=1}^{4} \sum_{j=1}^{4} a_{ij}}; \quad (26)$$

$$\text{Precision}_k = \frac{TP_k}{TP_k + FP_k} = \frac{a_{kk}}{\sum_i a_{ik}}; \quad (27)$$

$$\text{Recall}_k = \frac{TP_k}{TP_k + \sum_{j=1}^{4} FN_j} = \frac{a_{kk}}{\sum_j a_{kj}}; \quad (28)$$

$$\text{F1-Score} = 2 \times \frac{\text{Precision}_k \times \text{Recall}_k}{\text{Precision}_k + \text{Recall}_k}; \quad (29)$$

The classification report of our algorithms is being calculated by using these confusion matrices.

**B. Model Selection and Justification for the Classification Stage**

The proposed Twin-View hybrid framework comprises both classification and segmentation algorithms. In medical image analysis, the choice of a model must be guided not only by accuracy but also by stability, generalization, computational efficiency, and compatibility with downstream tasks, such as segmentation. Based on a literature review that establishes the research baseline, we have selected four algorithms. These algorithms are compared by their classification report to select the best one for the Twin-View model.

Although the ResNet-50 model achieved the highest overall classification accuracy of 94%, the Random Forest (RF) classifier was selected as the primary classification model due to several critical methodological and practical considerations.

Table 3 reveals that ResNet-50 slightly outperforms Random Forest in overall accuracy (0.94 vs. 0.90). The performance difference between the two models is quite small when assessed using class-based metrics. There are several factors to consider when choosing a Random Forest classifier, but one of the key factors is its stability and generalization. The Random Forest algorithm is an ensemble technique that combines the output of several decision trees. It reduces the variance and prevents overfitting. This property is especially valuable in medical datasets, where the number of training samples is often limited, and class distributions may be imbalanced.

Another reason is that the Random Forest classifier utilizes a hybrid feature vector composed of Histogram of Oriented Gradients (HOG) and Local Binary Patterns (LBP), which capture both structural and textural characteristics of MRI images. Each decision tree uses a randomly selected subset of features from the dataset, allowing the algorithm to identify the most valuable variables without performing any dimensionality reduction. Besides, interpretability is another important factor to consider. The classification report of our algorithms is shown in Table 3:

Table 3: Class-specific and overall performance metrics of evaluated deep learning and classical machine learning models for multi-class brain tumor classification.

| Model | Class | Precision | Recall | F1-score | Accuracy |
|---|---|---|---|---|---|
| ResNet50 | Glioma | 0.97 | 0.91 | 0.94 | 0.94 |
| | Meningioma | 0.95 | 0.99 | 0.97 | |
| | Non-tumor | 0.97 | 0.95 | 0.96 | |
| | Pituitary | 0.92 | 0.90 | 0.91 | |

| | | | | | |
|---|---|---|---|---|---|
| KNN | Glioma | 0.83 | 0.84 | 0.83 | 0.90 |
| | Meningioma | 0.84 | 0.98 | 0.91 | |
| | Non-tumor | 0.97 | 0.98 | 0.97 | |
| | Pituitary | 0.89 | 0.88 | 0.89 | |
| SVM | Glioma | 0.83 | 0.84 | 0.83 | 0.86 |
| | Meningioma | 0.84 | 0.97 | 0.90 | |
| | Non-tumor | 0.96 | 0.91 | 0.90 | |
| | Pituitary | 0.84 | 0.95 | 0.89 | |
| Random Forest | Glioma | 0.92 | 0.77 | 0.84 | 0.90 |
| | Meningioma | 0.84 | 0.97 | 0.90 | |
| | Non-tumor | 0.96 | 0.96 | 0.96 | |
| | Pituitary | 0.82 | 0.96 | 0.89 | |

Another reason is that the Random Forest classifier utilizes a hybrid feature vector composed of Histogram of Oriented Gradients (HOG) and Local Binary Patterns (LBP), which capture both structural and textural characteristics of MRI images. Each decision tree uses a randomly selected subset of features from the dataset, allowing the algorithm to identify the most valuable variables without performing any dimensionality reduction. Besides, interpretability is another important factor to consider.

**C. Learning Curves**

Fig. 15 illustrates the training and validation accuracy of the updated ResNet50 model throughout 30 epochs. The model's accuracy on the training set progressively rose and stabilized at 99%, whereas the validation accuracy exhibited fluctuations yet continuously remained elevated, converging between 85% and 90\% in the later epochs. This signifies that the model effectively acquired distinguishing features from the MRI images while preserving generalization on novel input. This indicates that the model successfully learned discriminative features from the MRI images while maintaining generalization on unseen data.

Likewise, Fig. 16 illustrates the training and validation loss trajectories. The training loss steadily diminished, indicating successful optimization of the model on the training dataset. The validation loss demonstrated fluctuations across epochs, a common occurrence in medical imaging tasks with very limited and imbalanced datasets. Notwithstanding the fluctuations, there was no substantial increase in validation loss, and the overall disparity between training and validation losses remained small, indicating that the model successfully evaded pronounced overfitting.

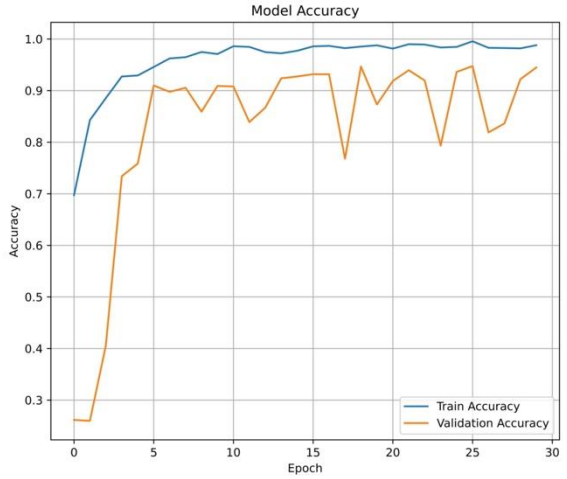


Fig. 15: Epoch-wise training and validation accuracy trajectories for the ResNet50 classification model.

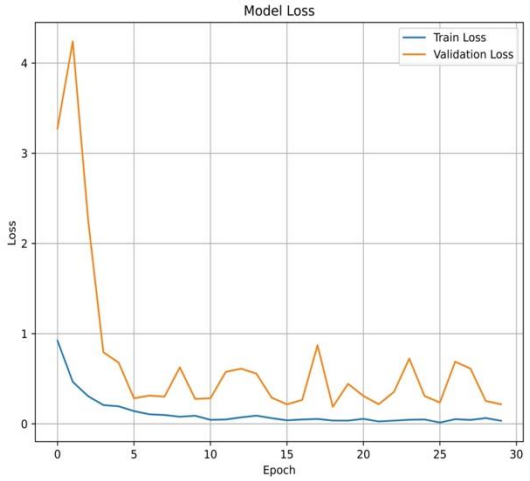


Fig. 16: Convergence profile of training and validation loss function values across training epochs for the ResNet50 model.

Fig. 17. illustrates the learning curves for the U-Net segmentation model, depicting the trends in loss and accuracy throughout 20 training epochs. The training and validation loss curves (right panel) demonstrate a consistent and gradual decline over time, ultimately converging to values beneath 0.04. This demonstrates the efficient reduction of the binary cross-entropy loss function employed in pixel-level tumor segmentation. The close proximity of training and validation loss indicates that the model generalizes effectively to unknown data and is not prone to overfitting.

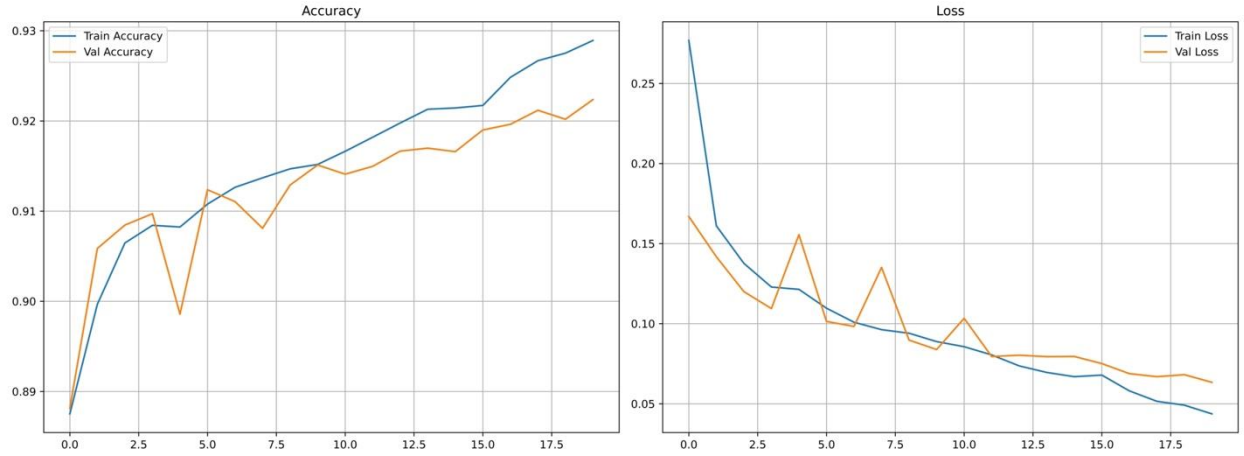


Fig. 17: Training and validation learning curves for the U-Net architecture: Dual-panel plot depicting epoch-wise transitions in classification accuracy and objective loss values.

The left panel displays the training and validation accuracy curves, which show a steady and incremental rise, with training accuracy nearing 93% and validation accuracy stabilizing at roughly 92%. The minimum gap between the two curves indicates consistency and implies that the model acquires robust characteristics applicable to the validation set. This pattern suggests that the U-Net has attained convergence without oscillations or instability, typically signifying an optimally adjusted learning rate and batch size.

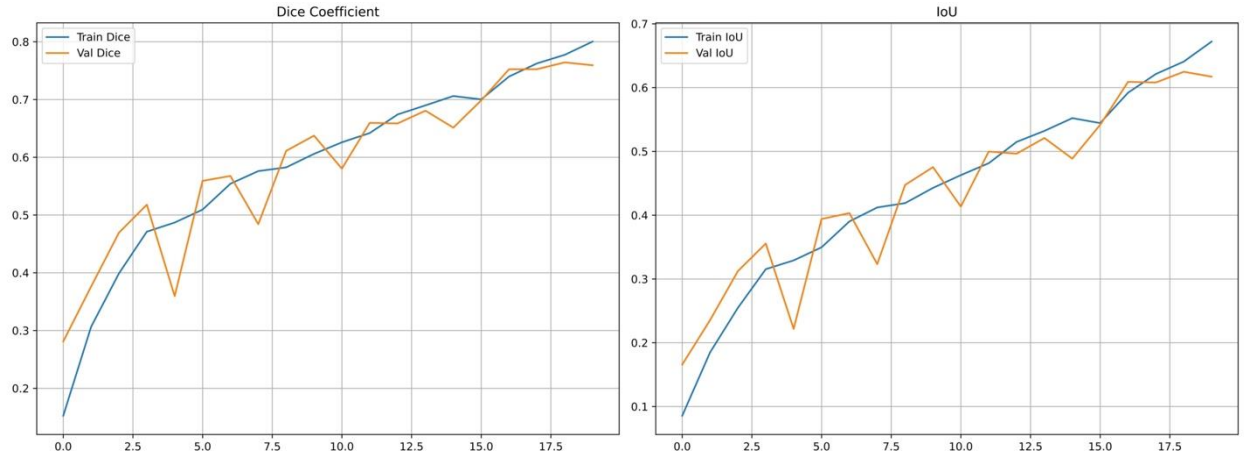


Fig. 18: Epoch-wise tracking of Dice coefficient and Intersection over Union (IoU) curves for the U-Net segmentation framework.

Fig. 18 represents the evolution of the Dice coefficient and Intersection over Union (IoU) metrics for training and validation sets throughout the U-Net model training. These metrics provide a more granular and task-specific measure of segmentation performance, particularly suited for medical image analysis where precise region boundaries are essential. As shown in the left panel, the Dice coefficient starts around 0.15 and improves steadily across epochs, eventually reaching approximately 0.80 for training and 0.75 for validation. This strong upward trend indicates that the model consistently learns to maximize the overlap between the predicted and ground truth tumor masks. The minimal gap between the training and validation Dice curves confirms that the model generalizes well, with little sign of overfitting. Similarly, the IoU curves (right panel) consistently increase over the epochs, with training IoU reaching around 0.70 and validation IoU stabilizing near 0.62. The convergence of both curves indicates that the model not only captures the presence of tumor regions but also aligns well with their precise boundaries, making it suitable for accurate medical segmentation tasks.

The overall trajectory of Dice and IoU metrics affirms the effectiveness of U-Net's encoder-decoder structure with skip connections in learning complex spatial relationships. High Dice and IoU values approaching 0.8 and 0.7, respectively, reflect a strong segmentation capability, validating the model's robustness in detecting and delineating tumor regions from 2D brain MRI images.

### D. Decision Boundary

A decision boundary represents the boundary that separates different classes or categories in a feature space. The model determines it during training and defines where one class transitions into another. The clarity and position of the decision boundary influence a model's ability to classify new instances accurately, as illustrated in Figs. 19 to 21.

Support Vector Machines (SVMs) often provide better decision boundaries in certain cases compared to k-Nearest Neighbors (KNN) or Random Forests due to their ability to find a hyperplane that maximally separates different classes. SVM aims to maximize the margin between classes, which can lead to better generalization to unseen data.

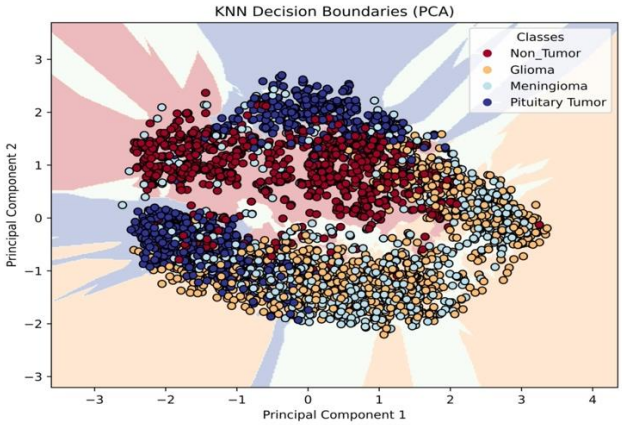


Fig. 19: K-Nearest Neighbors (KNN) decision boundaries projected onto the first two principal components ($\boldsymbol{PC_1}$ and $\boldsymbol{PC_2}$) of the texture feature space.

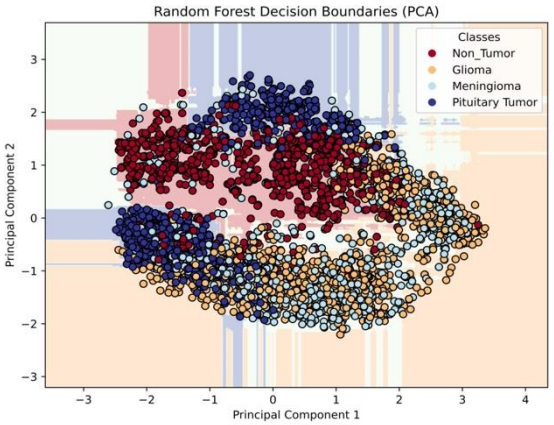


Fig. 20: Decision surface and partition boundaries generated by the Random Forest classifier within the reduced PCA feature dimensions.

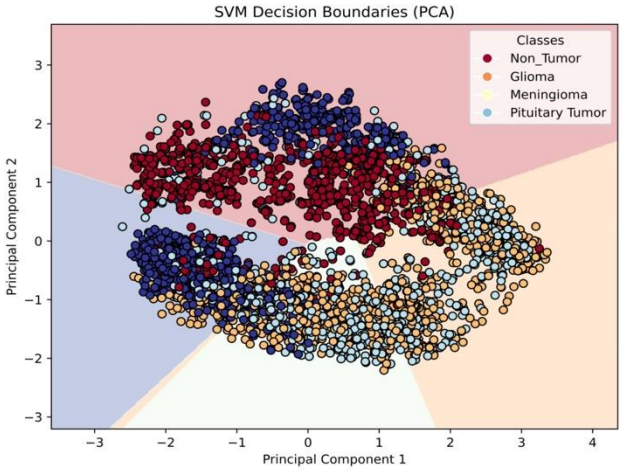


Fig. 21: Multi-class Support Vector Machine (SVM) decision boundaries illustrating hyper-plane partitioning on the $\boldsymbol{PC_1}$ versus $\boldsymbol{PC_2}$ feature plane.

**E. Segmentation and Classification Hybrid model result**

Table 4: Exemplar brain tumor segmentation and classification outputs for different pathological classes.

| Original Image | Binary Mask | Segmented Tumor | Tumor Type |
|---|---|---|---|
| 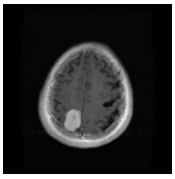 | 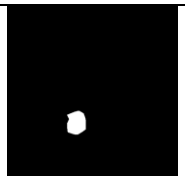 | 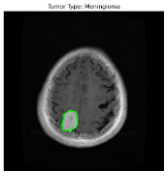 | **Meningioma** |
| 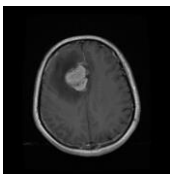 |  | 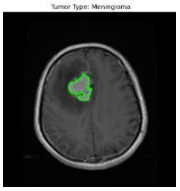 | **Meningioma** |
| 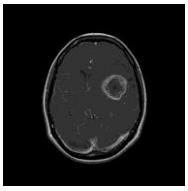 | 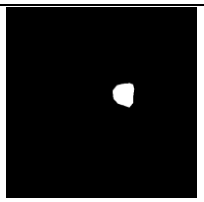 | 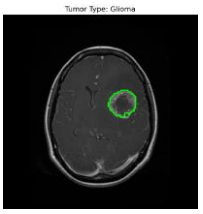 | **Glioma** |
| 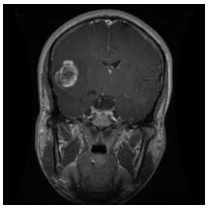 |  | 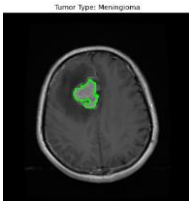 | **Glioma** |
| 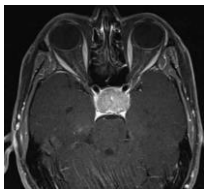 | 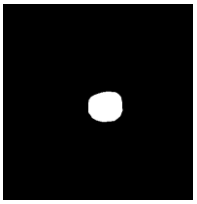 | 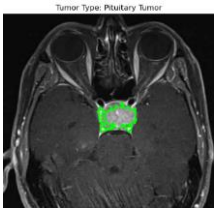 | **Pituitary tumor** |
| 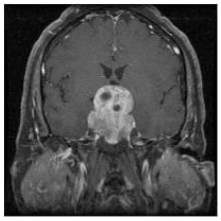 | 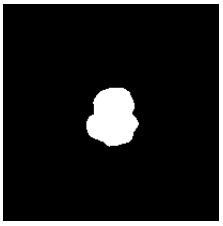 | 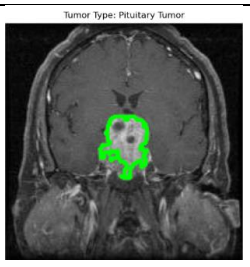 | **Pituitary tumor** |

The "Tumor Type" column in Table 4 presents the final classification output from the hybrid "Twin-View" framework. This result is generated by the Random Forest classifier component of the model, which determines the specific category of the tumor (e.g., Glioma, Meningioma, or Pituitary Tumor) for each MRI image. By

providing this definitive label, the column complements the visual segmentation shown in the "Segmented Tumor" column, offering a complete diagnostic output that includes both the location and type of the detected brain tumor.

### F. Comparison of the proposed 'Twin-View' with alternative models

Our suggested approach employs both classification and segmentation methodologies to identify the tumor. Previous studies have developed alternative approaches, such as MLP and NB algorithm [28], Deep neural network [14] and CNN [30] that utilize binary classification to differentiate between tumor and non-neoplastic brain pictures. Mathaiyalagan and Devaraj [37] presents a model capable of exclusively detecting Glioma. Our model can identify three distinct tumor variants: Glioma, Meningioma, and Pituitary Tumor, positioning it superior to other models.

### G. Model check with real-time image

We have collected an MRI image from a hospital. The image contains tumor slices of different axes in Fig. 22. After providing that to our model, the model has successfully predicted the tumor class. The MRI image is collected from a healthy person, and our model successfully predicted that in Fig. 23.

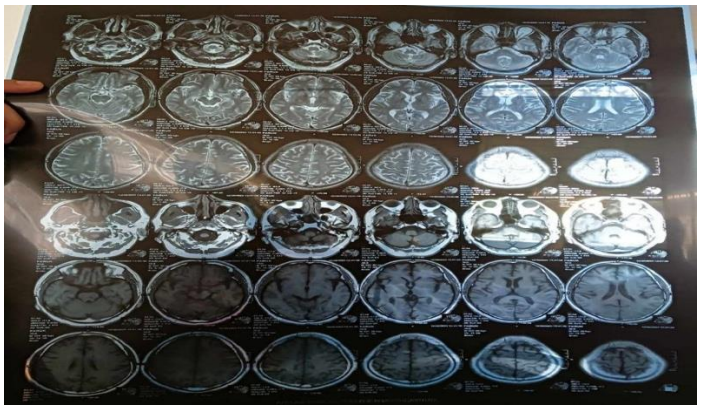

Fig. 22: Representative sample of the digitized raw multi-slice clinical MRI film dataset collected for independent validation.

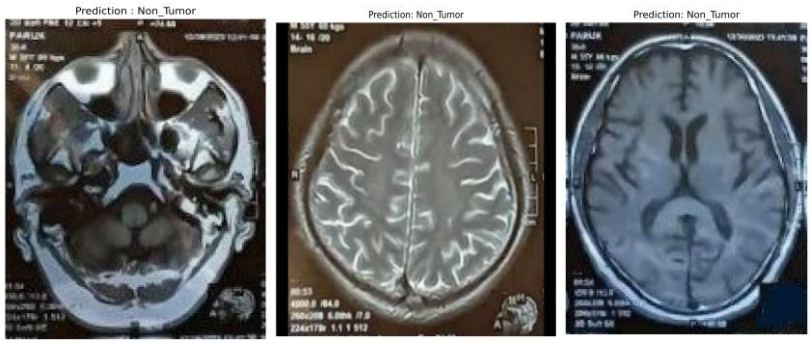


Fig. 23: Individual axial slices extracted from the clinical dataset and their corresponding model inference outputs indicating diagnostic class predictions.

## 4. Conclusion

The proposed "Twin-View" framework addresses the critical need for a comprehensive and automated system for brain tumor analysis by integrating both segmentation and classification functionalities. Unlike many existing studies that focus on either classification or segmentation alone, our hybrid model provides a cohesive solution that offers both a definitive tumor class and a precise visual localization of the tumor region. The research employed a modified ResNet50 architecture and machine learning models (KNN, SVM, and Random Forest) for classification, as well as a U-Net model for pixel-level segmentation.

Our findings confirm the effectiveness of this hybrid approach. The U-Net model demonstrated strong performance in segmentation, with high Dice and IoU scores (approximately 0.8 and 0.7, respectively), indicating its ability to accurately delineate tumor boundaries. For classification, the ResNet50 model achieved the highest standalone accuracy at 94%, while the Random Forest classifier, chosen for its compatibility with the hybrid pipeline, also performed well with 90% accuracy. The "Twin-View" framework successfully uses the U-Net's segmentation output to inform and enhance the Random Forest classification, providing a complete diagnostic output that

includes the tumor type and its precise location on the MRI image. The model was also successfully tested with real-time MRI images, correctly identifying both a non-tumor case and a tumor case, demonstrating its potential for real-world clinical application. The ability to classify three distinct tumor variants, glioma, meningioma, and pituitary tumor, sets this model apart from other approaches that only perform binary classification or detect a single type of tumor. This comprehensive, two-pronged analysis provides a valuable tool that can assist medical professionals in making faster, more accurate diagnoses.

**Data Availability Statement**

The original dataset can be accessed directly at the following URL: Msoud Nickparvar. (2026). Brain Tumor MRI Dataset [Dataset]. Kaggle. https://doi.org/10.34740/KAGGLE/DSV/14832123 [41].

**Acknowledgment**

This research was funded and supported by the Research and Extension Center of Jatiya Kabi Kazi Nazrul Islam University under the research grant for the fiscal year 2024–2025. The authors gratefully acknowledge the financial and administrative assistance provided by the institution.

**References**

[1] Patel, Benign vs Malignant Tumors, JAMA Oncology, 6(9), 2020 1488, https://doi.org/10.1001/jamaoncol. 2020.2592.
[2] J. H. Sampson, M. D. Gunn, P. E. Fecci, D. M. Ashley, Brain immunology and immunotherapy in brain tumours, Nature Reviews Cancer, 20(1), 2020, 12–25.
[3] S.Schmidgall, R.Ziaei, J.Achterberg, L.Kirsch, S.P.Hajiseyedrazi, J. Eshraghian, Brain-inspired learning in artificial neural networks: A review, APL Machine Learning, 2(2), 2024, https://doi.org/10.1063/5.0186054
[4] R.A.Weinberg, R.A.Weinberg, The biology of cancer, WW Norton & Company, 2006.
[5] S. E. Amin, M. Megeed, Brain tumor diagnosis systems based on artificial neural networks and segmentation using MRI, 8th International Conference on Informatics and Systems (INFOS), IEEE, 2012, pp. 119-124.
[6] Sarkar, S. C. and B. D. and Y. T. and A. M. B. and F. S. (2021). Brain Tumor Spectrum of Patient Attending at a Tertiary Care Hospital in Bangladesh. EAS Journal of Radiology and Imaging Technology. Https://Easpublisher. Com/Media/Features_articles/EASJRIT_35_255-258. Pdf.
[7] Rahman, M. L., Ali, A. S., Islam, M. S., Alam, I., & Mohiuddin, A. (2011). Brain Tumors - Analysis of 320 Cases. TAJ: Journal of Teachers Association, 19(1), 24–26. https://doi.org/10.3329/taj.v19i1.3164
[8] Sharma, N., Gupta, S., Koundal, D., Alyami, S., Alshahrani, H., Asiri, Y., & Shaikh, A. (2023). U-Net Model with Transfer Learning Model as a Backbone for Segmentation of Gastrointestinal Tract, Bioengineering, 10(1), 119. https://doi.org/10.3390/bioengineering10010119
[9] Shen, G., Hao, B., Li, M., Farris, C. W., Paschalidis, I. Ch., Anderson, S. W., & Zhang, X. (2023). Attention hybrid variational net for accelerated MRI reconstruction. APL Machine Learning, 1(4). https://doi.org/10.1063/5.0165485
[10] Aslam, A., Khan, E., & Beg, M. M. S. (2015). Improved Edge Detection Algorithm for Brain Tumor Segmentation. Procedia Computer Science, 58, 430–437. https://doi.org/10.1016/j.procs.2015.08.057
[11] Gardner, K., Joshi, R., Hasan Kashem, M. N., Pham, T. Q., Lu, Q., & Li, W. (2023). Label free identification of different cancer cells using deep learning-based image analysis. APL Machine Learning, 1(2). https://doi.org/10.1063/5.0141730
[12] Wu, D. H. (2020). Machine learning paradigm for dynamic contrast-enhanced MRI evaluation of expanding bladder. Frontiers in Bioscience, 25(9), 4876. https://doi.org/10.2741/4876
[13] Damodharan, S. and R. D. (2015). Combining tissue segmentation and neural network for brain tumor detection. International Arab Journal of Information Technology (IAJIT), 12, 42–52.
[14] Choudhury, C. L., Mahanty, C., Kumar, R., & Mishra, B. K. (2020). Brain Tumor Detection and Classification Using Convolutional Neural Network and Deep Neural Network. 2020 International Conference on Computer Science, Engineering and Applications (ICCSEA), 1–4. https://doi.org/10.1109/ICCSEA49143.2020.9132874
[15] Zacharaki, E. I., Wang, S., Chawla, S., Soo Yoo, D., Wolf, R., Melhem, E. R., & Davatzikos, C. (2009). Classification of brain tumor type and grade using MRI texture and shape in a machine learning scheme. Magnetic Resonance in Medicine, 62(6), 1609–1618. https://doi.org/10.1002/mrm.22147
[16] Bauer, S., Wiest, R., Nolte, L.-P., & Reyes, M. (2013). A survey of MRI-based medical image analysis for brain tumor studies. Physics in Medicine and Biology, 58(13), R97–R129. https://doi.org/10.1088/0031-9155/58/13/R97
[17] Krizhevsky, A., Sutskever, I., & Hinton, G. E. (2017). ImageNet classification with deep convolutional neural networks. Communications of the ACM, 60(6), 84–90. https://doi.org/10.1145/3065386
[18] Shafiq, M., & Gu, Z. (2022). Deep Residual Learning for Image Recognition: A Survey. Applied Sciences, 12(18), 8972. https://doi.org/10.3390/app12188972
[19] Esteva, A., Kuprel, B., Novoa, R. A., Ko, J., Swetter, S. M., Blau, H. M., & Thrun, S. (2017). Dermatologist-level classification of skin cancer with deep neural networks. Nature, 542(7639), 115–118. https://doi.org/10.1038/nature21056
[20] Elpeltagy, M., & Sallam, H. (2021). Automatic prediction of COVID− 19 from chest images using modified ResNet50. Multimedia Tools and Applications, 80(17), 26451–26463. https://doi.org/10.1007/s11042-021-10783-6
[21] Younis, A., Li, Q., Afzal, Z., Jajere Adamu, M., Bello Kawuwa, H., Hussain, F., & Hussain, H. (2024). Abnormal Brain Tumors Classification Using ResNet50 and Its Comprehensive Evaluation. IEEE Access, 12, 78843–78853. https://doi.org/10.1109/ACCESS.2024.3403902
[22] Bastug Koc, A., & Akgun, D. (2026). A Review of U-Net Based Deep Learning Frameworks for MRI-Based Brain Tumor Segmentation. Diagnostics (Basel, Switzerland), 16(4). https://doi.org/10.3390/diagnostics160 40506

[23] Siddique, N., Paheding, S., Elkin, C. P., & Devabhaktuni, V. (2021). U-Net and Its Variants for Medical Image Segmentation: A Review of Theory and Applications. IEEE Access, 9, 82031–82057. https://doi.org/10.1109/ACCESS.2021.3086020
[24] Rehman, M. U., Cho, S., Kim, J. H., & Chong, K. T. (2020). BU-Net: Brain Tumor Segmentation Using Modified U-Net Architecture. Electronics, 9(12), 2203. https://doi.org/10.3390/electronics9122203
[25] Cao, H., Tao, L., Li, F., & Pan, X. (2026). Efficient transformer integration in nnU-Net for liver tumor segmentation: an external validation study. BMC Medical Imaging. https://doi.org/10.1186/s12880-026-02406-z
[26] Chen, K., Wang, Y., & Cheng, J. (2026). NFM-Nest: Neighbour fusion and residual fusion networks for medical image segmentation. Biomedical Signal Processing and Control, 113, 109150. https://doi.org/10.1016/j.bspc.2025.109150
[27] Punn, N. S., & Agarwal, S. (2022). Modality specific U-Net variants for biomedical image segmentation: a survey. Artificial Intelligence Review, 55(7), 5845–5889. https://doi.org/10.1007/s10462-022-10152-1
[28] Sharma, K., Kaur, A., & Gujral, S. (2014). Brain Tumor Detection based on Machine Learning Algorithms. International Journal of Computer Applications, 103(1), 7–11. https://doi.org/10.5120/18036-6883
[29] Kshirsagar, P. R. and R. A. N. and C. P. (2020). MRI image based brain tumor detection using machine learning. Test Engineering and Management, 81, 3672–3680.
[30] Siddique, M. A. B. and S. S. and K. M. M. R. and T. A. K. and C. M. and Y. N. (2020). Deep convolutional neural networks model-based brain tumor detection in brain MRI images. 2020 Fourth International Conference on I-SMAC (IoT in Social, Mobile, Analytics and Cloud)(I-SMAC), 909–914.
[31] Abdusalomov, A. B., Mukhiddinov, M., & Whangbo, T. K. (2023). Brain Tumor Detection Based on Deep Learning Approaches and Magnetic Resonance Imaging. Cancers, 15(16), 4172. https://doi.org/10.3390/cancers15164172
[32] Sadad, T., Rehman, A., Munir, A., Saba, T., Tariq, U., Ayesha, N., & Abbasi, R. (2021). Brain tumor detection and multi-classification using advanced deep learning techniques. Microscopy Research and Technique, 84(6), 1296–1308. https://doi.org/10.1002/jemt.23688
[33] Sajid, S., Hussain, S., & Sarwar, A. (2019). Brain Tumor Detection and Segmentation in MR Images Using Deep Learning. Arabian Journal for Science and Engineering, 44(11), 9249–9261. https://doi.org/10.1007/s13369-019-03967-8
[34] Jia, Z., & Chen, D. (2025). Brain Tumor Identification and Classification of MRI Images Using Deep Learning Techniques. IEEE Access, 13, 123783–123792. https://doi.org/10.1109/ACCESS.2020.3016319
[35] Methil, A. S. (2021). Brain Tumor Detection using Deep Learning and Image Processing. 2021 International Conference on Artificial Intelligence and Smart Systems (ICAIS), 100–108. https://doi.org/10.1109/ICAIS50930.2021.9395823
[36] Amin, J., Sharif, M., Raza, M., & Yasmin, M. (2024). Detection of Brain Tumor based on Features Fusion and Machine Learning. Journal of Ambient Intelligence and Humanized Computing, 15(1), 983–999. https://doi.org/10.1007/s12652-018-1092-9
[37] Mathiyalagan, G., & Devaraj, D. (2021). A machine learning classification approach based glioma brain tumor detection. International Journal of Imaging Systems and Technology, 31(3), 1424–1436. https://doi.org/10.1002/ima.22590
[38] Pan, P., Zhang, C., Sun, J., & Guo, L. (2025). Multi-scale conv-attention U-Net for medical image segmentation. Scientific Reports, 15(1), 12041. https://doi.org/10.1038/s41598-025-96101-8
[39] Lu, D., Xu, L., Zhou, J., Gao, K., Gong, Z., & Zhang, D. (2025). 3D-UMamba: 3D U-Net with state space model for semantic segmentation of multi-source LiDAR point clouds. International Journal of Applied Earth Observation and Geoinformation, 136, 104401. https://doi.org/10.1016/j.jag.2025.104401
[40] Sanker, V., Mahesh, D., Li, Z., Thaller, A., Heesen, P., Liverani, L., Wang, D., Cavagnaro, M. J., Medikonda, R. T., Prolo, L., Singh, H., Ratliff, J., & Desai, A. (2026). 3D Deep Learning for Brain Tumor Segmentation and Survival Prediction: A Comprehensive Multi-Modal Analysis Using the BraTS2020 Dataset. Journal of Imaging, 12(6), 251. https://doi.org/10.3390/jimaging12060251
[41] Msoud Nickparvar. (2026). Brain Tumor MRI Dataset [Dataset]. Kaggle. https://doi.org/10.34740/KAGG LE /DSV/14832123